Canadian
Science
Publishing

ARTICLE

Experimental analysis of rolling dynamic compaction using transparent soils and particle image velocimetry

Yue Chen, Mark B. Jaksa, Yien-Lik Kuo, and David W. Airey

Abstract: Rolling dynamic compaction (RDC) is a soil compaction technique, which is capable of improving thick layers of soil at a relatively fast operating speed. The paper presents the results of laboratory experiments conducted on 1:13 scale models of the four-sided, 8 and 12 t, Broons BH-1300 and BH-1300 HD impact rollers, respectively, to study the performance of the scale model at four different operating speeds. A series of laboratory tests is undertaken using transparent soils and the particle image velocimetry (PIV) technique to investigate the effectiveness of the models. The transparent soil employed in this study consists of fused quartz and a pore fluid that matched the refractive index of the fused quartz. A one-particle thick layer of coloured fused quartz is embedded in the centre plane of the transparent soil to visualize soil internal displacements and a digital camera is used to capture the speckled pattern during the scale model testing process. The results show that the heavier module induces greater soil displacements at each operating speed. The optimal operating speed is approximately 299 mm/s for both module weights. The most significant soil displacements occur within the first 20 passes and no obvious ground improvement is observed after 35 passes. The results of this study demonstrate the unique capability of transparent soil to study soil displacements induced by the ground improvement scale models.

Key words: rolling dynamic compaction, impact roller, ground improvement, transparent soil, particle image velocimetry.

Résumé : Le compactage dynamique par roulement (CDR) est une technique de compactage du sol, capable d'améliorer des couches épaisses de sol à une vitesse de fonctionnement relativement rapide. L'article présente les résultats d'expériences de laboratoire menées sur des modèles à l'échelle 1:13 des rouleaux d'impact Broons BH-1300 et BH-1300 HD à quatre côtés, de 8 et 12 t, respectivement, afin d'étudier les performances du modèle réduit à quatre vitesses de fonctionnement différentes. Une série d'essais en laboratoire est réalisée à l'aide de sols transparents et de la technique de vélocimétrie par images de particules (PIV) afin d'étudier l'efficacité des modèles. Le sol transparent utilisé dans cette étude se compose de quartz fondu et d'un fluide interstitiel dont l'indice de réfraction correspond à celui du quartz fondu. Une couche de quartz fondu coloré d'une épaisseur d'une particule est incorporée dans le plan central du sol transparent pour visualiser les déplacements internes du sol et un appareil photo numérique est utilisé pour capturer le motif moucheté pendant le processus d'essai du modèle réduit. Les résultats montrent que le module le plus lourd induit des déplacements de sol plus importants à chaque vitesse de fonctionnement. La vitesse optimale de fonctionnement est d'environ 299 mm/s pour les deux poids de modules. Les déplacements du sol les plus importants se produisent au cours des 20 premiers passages et aucune amélioration évidente du sol n'est observée après 35 passages. Les résultats de cette étude démontrent la capacité unique du sol transparent permettant d'étudier les déplacements du sol induits par les modèles d'amélioration du sol à l'échelle. [Traduit par la Rédaction]

Mots-clés : compaction dynamique par roulement, rouleau à impact, amélioration du sol, sol transparent, vélocimétrie par image de particules.

Introduction

The stability and serviceability of foundations are highly dependent on the bearing capacity and settlement of the underlying soil. With the global increase in population and the consequent growing demand for land for housing and development, construction on soft, weak, compressible, and filled ground is becoming increasingly prevalent. Hence, ground improvement has become an important and common component of civil engineering construction. Compaction is commonly employed as it is the most cost-effective ground improvement approach. The density of soil is improved by applying mechanical energy to reduce the volume of the voids.

Based on the type of compactive effort, compaction is divided into static and dynamic methods. Static compaction involves the densification of the ground by gradually applying the self-weight of heavy machinery. In contrast, dynamic compaction involves, in addition to self-weight, the application of repeated high energy impact forces.

Rolling dynamic compaction (RDC) is a form of dynamic compaction. It involves towing a heavy, non-circular module (typically 6–12 t and three-, four- or five-sided) behind a tractor, such that the module rotates about its corners and falls repeatedly to impact the ground. It improves the subsurface profile to a greater depth (1–3 m) when compared with conventional static and vibratory compaction. RDC is particularly efficient in large, open sites

as it can be operated at a greater speed (10–12 km/h) when compared with the 4 km/h of traditional compaction equipment (Pinard 1999). The deeper compactive depth and greater operating speed result in the extensive use of RDC in earthworks construction, such as, in situ densification of existing fills, large reclamation projects, reconstruction of rural roads, and mining and agricultural related applications (Avalle and Carter 2005; Avalle and McKenzie 2005; Bouazza and Avalle 2006). Because of the greater induced energy, ground vibrations generated during the compaction process may cause potential hazards to nearby structures, particularly those vulnerable to vibrations, such as older heritage structures. Therefore, a buffer zone of approximately 2–5 m is recommended for industrial buildings, and a 7–20 m zone is suggested for residential buildings when adopting the four-sided, 8 t module (Avalle 2007). In addition, Avalle (2006) reported that, the ground surface becomes undulating and the upper ground surface is loosened after RDC compaction due to the geometry of the module. Therefore, a grader and a conventional circular roller are generally used to level and compact the soil near the ground surface after the application of RDC.

Field tests have been undertaken to examine the energy transfer, the zone of influence, and the surface settlement of RDC (Jaksa et al. 2012; Scott and Jaksa 2014). As conducting field tests is costly and time-consuming, physical scale models have been utilized in controlled laboratory environments to quantify the performance of RDC with respect to different soil types, roller speeds and masses (Rajarathnam et al. 2016; Chung et al. 2017; Li et al. 2021). These studies have shown that physical scale models can produce similar ground response to that of the full-size modules. Previous studies are valuable for understanding the behaviour of RDC; however, it is difficult to assess the soil response, such as the internal soil displacement, depth of improvement, and ground settlement.

The internal deformation of soil within a mass under RDC has long been a topic of interest because soil displacements are considered as a direct indicator of the effectiveness of RDC. However, as natural soil is opaque, the displacement of soil within the soil body is difficult to observe and quantify. Accelerometers and earth pressure cells have been used in field (Scott et al. 2019) and scale model (Chung et al. 2017; Jaksa et al. 2019) testing in an effort to measure ground improvement. Soil displacements were calculated by double integrating the obtained acceleration with respect to time. The use of accelerometers is, however, an intrusive technology as they need to be embedded into the soil body at different depths to measure ground accelerations. Accelerometers are constructed using small metal plates that might affect the displacement response of the surrounding soil due to different material properties of the sensors with respect to the soil. Other technologies like radiography, computerized axial tomography (CAT), and magnetic resonance imaging (MRI) have been employed by several researchers to examine various geotechnical problems (e.g., Bransby and Milligan 1975; Mandava et al. 1990; Posadas et al. 1996), but these are limited in their ability to investigate rapid loading events. In addition, the cost of these tests is high and their experimental setup is challenging (Iskander 2010). With the advent of digital optical equipment and imaging science, transparent materials have been recently used to replace opaque soil particles in experimental tests. With the help of the particle image velocimetry (PIV) technique, transparent soil has been employed to study: (i) soil displacements under strip footings (Liu 2009; Liu and Iskander 2010); (ii) ground response due to tunnelling (Ahmed and Iskander 2012); and (iii) measure soil movements around pile foundations (Liu et al. 2010). Previous research has shown that transparent soil and PIV are appropriate for investigating soil displacement problems in geotechnical engineering.

In this paper, transparent soil, made of fused quartz and a matched refractive index (RI) pore fluid, was used to help study the performance of 1:13 scale modules of the four-sided, 8 and 12 t, Broons BH-1300 and BH-1300 HD impact rollers, respectively. The behaviour of the roller module is evaluated from four aspects: (i) the soil movement relative to the module motion; (ii) optimal operating speed; (iii) optimum number of rolling passes; and (iv) settlement of the ground surface. To assist in visualizing the internal displacement of the transparent soil, a small proportion of the fused quartz particles were painted black to form a one-particle thick layer of black particles in the transparent soil mass. This one-particle thick layer of coloured fused quartz was located along the centreline of the roller traverse lane, and with the transparent particles, formed a speckled pattern. The displacement of the pattern subjected to the impact roller was captured by a conventional charge-coupled device (CCD) camera. Images were then analysed by the PIV technique to investigate the displacement fields. Results obtained from the PIV technique were used to understand the mechanics and effectiveness of the roller module.

Experimental setup

This section presents the experimental setup and discusses the materials used, sample preparation, the PIV system, the experimental procedure, and the calibration tests.

Materials

Transparent soil is a two-phase medium, which contains solid transparent surrogates and a matched RI pore fluid. In this study, fused quartz (Fig. 1a) was chosen as the transparent surrogate. This material is stable, hard, and exhibits high transparency. The fused quartz particles were sieved before and after the scale model testing and the reduction in particle size was found to be insignificant in this study. A wide range of grain sizes is available commercially and high purity fused quartz particles are essential to obtain better visibility of the transparent soil. Considering the transparency of the particles and the size of the chamber, in this study, the fused quartz size range is selected to be between 3 and 5 mm, with mean particle size D_{50} equal to 3.84 mm (this is treated in greater detail in the following section). The particle-size distribution curve of the fused quartz particles is shown in Fig. 1b. Based on the Unified Soil Classification System (ASTM 2017), fused quartz is classified as a poorly graded fine gravel (GP). The RI of fused quartz is 1.458. The matching pore fluid used in this paper was sodium-thiosulfate treated sodium-iodide (STSI) solution, which was introduced by Carvalho et al. (2015). At 22 °C, the RI of sodium iodide and water are 1.77 and 1.33, respectively. The mixed solution, with the proportion of 105 g of sodium iodide per 100 mL water, has an RI value of 1.458 at 22 °C. The maximum and minimum void ratios of the fused quartz are 0.947 and 0.574, respectively. Figure 2 demonstrates the clarity of text printed on a sheet of white paper viewed behind a 60 mm thickness of fused quartz (Fig. 2a) and STSI saturated fused quartz (Fig. 2b). It can be seen that after the addition of STSI solution, the transparency of the fused quartz increases dramatically.

Sample preparation

Fused quartz was washed using distilled water to remove any impurities and subsequently dried in the oven. As the RI of the pore fluid varies with temperature, the STSI solution was prepared in the laboratory such that the temperature was maintained at approximately 22 °C. The RI of STSI pore fluid was measured after preparation by using a handheld refractometer.

A small proportion of fused quartz particles were painted matte black to prevent light transmission. The dyed particles were randomly and manually scattered between two thick layers of transparent soil to form a speckled pattern with unique texture. Particle displacements resulted in the changes of speckled pattern during the roller module travels. The movement of speckled pattern was captured by a CCD camera and then images were analysed by the PIV technique.

Fig. 1. (*a*) Fused quartz samples and (*b*) particle-size distribution curve. [Colour online.]
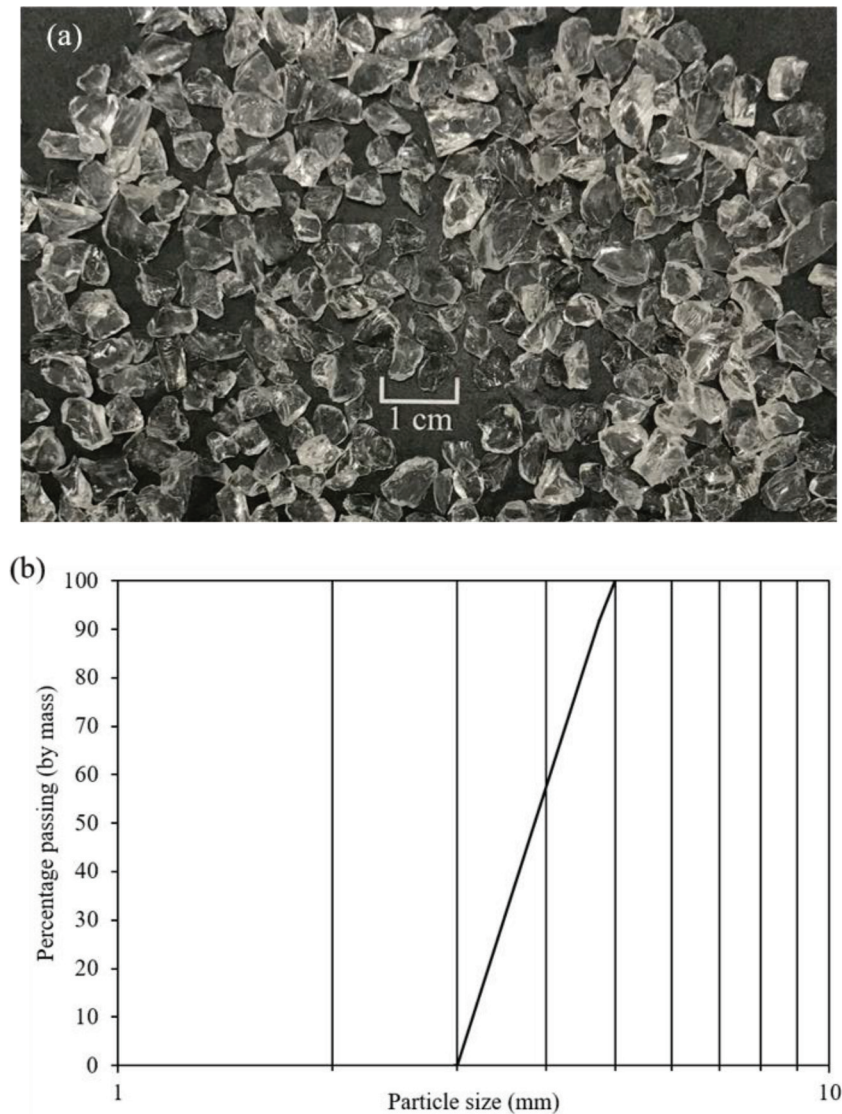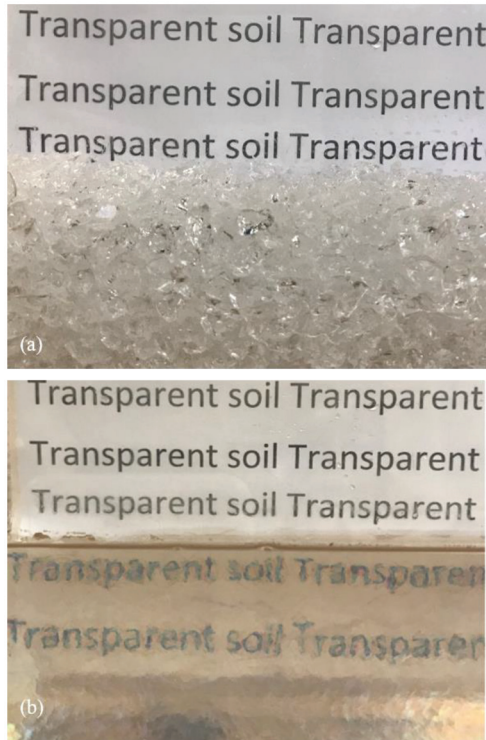

The transparent soil sample was prepared in an acrylic rectangular chamber, with dimensions of 300 mm × 280 mm × 250 mm (length × width × height). The chamber was constructed from 12 mm thick acrylic sheets with two detachable panels at its front and top sides to facilitate the placement of a thin layer of black-dyed fused quartz particles in the centre of the transparent soil sample (Fig. 3*a*). The front panel was removed and the transparent particles were carefully placed in the chamber, first by tipping the chamber on its side (Fig. 3*b*). The STSI solution was poured into the box, prior to pluviating the particles to minimize the formation of air bubbles. To achieve consistent density, the fused quartz particles were pluviated in successive layers from the same approximate height of 50 mm, until half of the chamber was filled (i.e., 140 mm). The surface of the transparent soil sample was then carefully levelled. Black-dyed particles were subsequently placed to generate a distributed speckled pattern. The remaining half of the chamber was then filled with fused quartz particles in the same manner as previously described. The front panel was then replaced and the chamber was tipped back into its normal orientation (from Figs. 3*a* and 3*b*). The top panel was removed in readiness for testing. Prior to testing, the transparent soil surface was carefully levelled. The initial void ratio of the fused quartz was 0.728, which yielded a relative density of 58.7%.

In practice, dynamic compaction, as well as RDC, is best performed on soils with moisture contents at or below the optimum moisture content (Scott et al. 2012). However, in the present study, given that the fused quartz is required to be fully saturated to achieve sample transparency, optimum moisture content is irrelevant. The application of dynamic compaction on saturated soils is presently a controversial topic. Some researchers, such as Pak et al. (2005) and Bo et al. (2009), have commented that the compactive effort induced by dynamic compaction resulted in an increase in pore-water pressure. The high pore-water pressure either reduced the effectiveness of dynamic compaction in the impervious saturated soils (e.g., clayey soils with a plasticity index larger than 8) or caused liquefaction in sandy soils. However, Pak et al. (2005) stated that dynamic compaction is effective on saturated soils if the soil is free draining, as the pore water has low compressibility when compared with the soil skeleton. In the present study, drainage occurs at the top surface to facilitate soil compaction. More importantly, however, and whilst not entirely ideal, in the present study the soil is saturated to facilitate soil transparency. As demonstrated in the paper, the transparent

Fig. 2. Transparent soil with text viewed from behind 60 mm thickness of fused quartz with (*a*) no pore fluid and (*b*) STSI pore fluid. [Colour online.]

Fig. 3. Acrylic chamber placed (*a*) in its testing orientation and (*b*) on its side to facilitate placement of the transparent surrogates. [Colour online.]
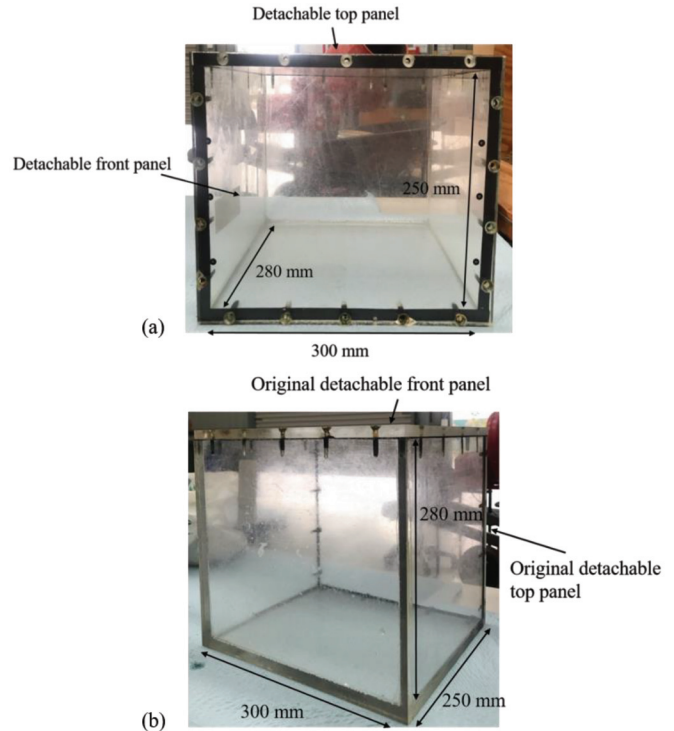

nature of the soil provides great insight into RDC-induced ground improvement.

Particle image velocimetry (PIV) system

When the roller module traverses and compacts the simulated ground surface, the particles displace and, given the transparent nature of soil, along with the central plane of speckled particles, displacements can be observed and measured using the PIV technique. Images before and throughout the roller module process were captured using a conventional CCD camera. In this study, a 2.3 megapixel, monochrome Point Grey CCD camera was used. It can capture up to 163 frames per second at 1920 × 1200 pixel resolution. As the centreline of the traverse of the module is coincident with the centreline of the chamber, and hence the speckle-patterned plane, the displacement of the black-dyed particles is assumed to be a plane-strain problem, and therefore only a single camera was needed and used. The lens adopted in this study was a Schneider–Kreuznach Xenoplan f/1.4 with a 17 mm focal length. The camera was placed in front of the chamber and the distance between the lens and the chamber was maintained at 800 mm for all tests. "VicSnap" is a commercial computer program, which connects the camera to the computer for image acquisition purposes. This software also provides a preview of the captured images for users and it allows users to adjust the imaging parameters remotely, such as the area of interest, resolution, exposure times, and frame rate. In this study, all images were captured with full resolution (1920 × 1200 pixels) at 120 frames per second.

PIV is an image-based technique that was first applied in fluid mechanics by Adrian (1991) to obtain velocity changes. The texture of an image is tracked by the PIV technique through a series of images to obtain displacement fields. In this study, PIV analysis was conducted using a free MATLAB module "GeoPIV_RG" developed by Stanier et al. (2016). GeoPIV_RG adopts the first-

order subset shape function to gather subpixel resolution displacements, which increases precision and reduces random walk errors (Stanier et al. 2016).
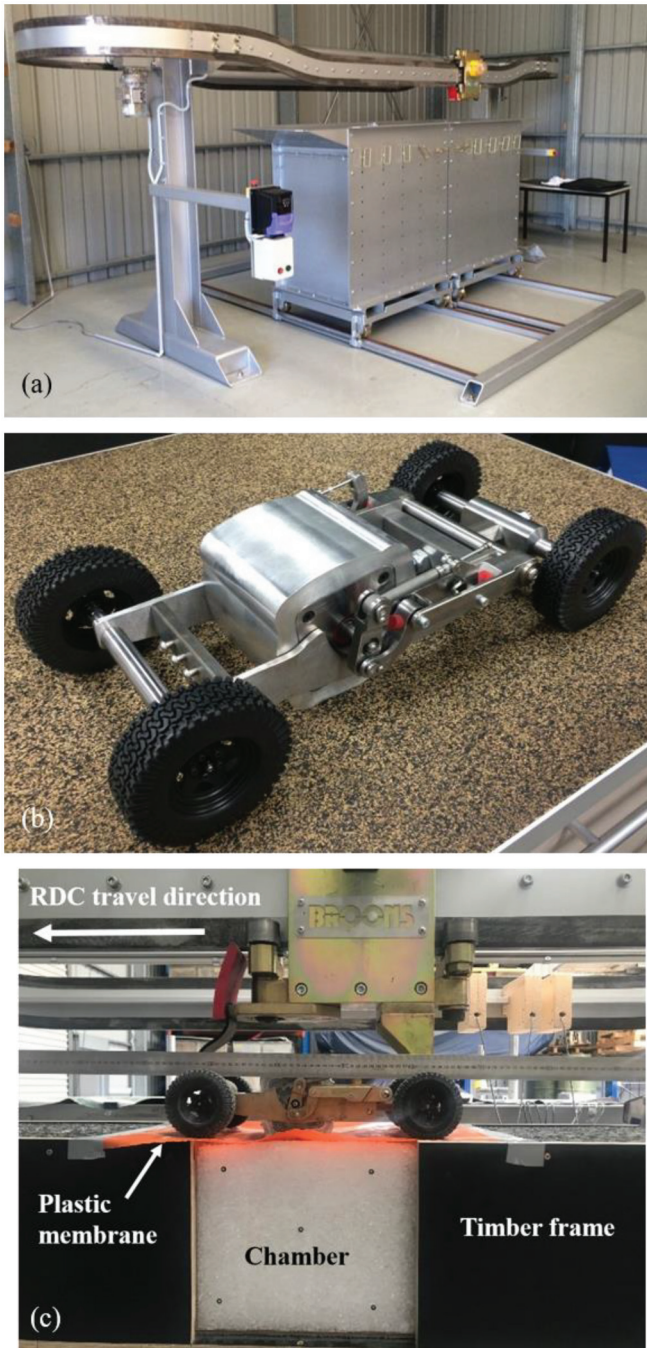
Experimental procedure

A bespoke test facility was developed to facilitate the RDC-related research program. The testing equipment incorporates a stadium-shaped track (Fig. 4a). A variable-speed electric motor pulls a 1:13 scale model of the four-sided impact roller (Fig. 4b) around the track and across the transparent soil filled chamber that is housed within a timber frame (Fig. 4c). The 1:13 scale ratio was selected as an optimal compromise between the overall dimensions and weights of the test rig, operation accuracy, employed soil particle size, and fabrication costs. Several tests were performed by Chung et al. (2017) using this test facility with a sandy gravel soil with maximum particle sizes of 10 mm. The results from the 1:13 scale model were in good agreement with field test measurements obtained by Scott et al. (2016) using the full-size impact roller over the same soil and no particle size effects were detected, which suggests the 1:13 scale model is a reliable surrogate for the full-size RDC module.

The scale model was designed and fabricated so that its density is identical to the full-size model. The scaling laws developed by Altaee and Fellenius (1994) (eqs. 1–6), for scale model testing under a normal gravity (1g) situation, were used to correlate the properties of the scale model with those of the full-size model. In this study, the geometric scale ratio (*n*) is 1/13.

$$(1) \qquad \frac{L_m}{L_p} = n$$

$$(2) \qquad \frac{V_m}{V_p} = n^3$$

Fig. 4. RDC experimental facility: (*a*) test rig, (*b*) 1:13 scale model of four-sided impact roller, and (*c*) transparent soil setup. [Colour online.]

(a)

(b)

RDC travel direction

BROOMS

Plastic
membrane

Chamber

Timber frame

(c)

$$(3) \quad \frac{M_{\mathrm{m}}}{M_{\mathrm{p}}} = n^3$$

$$(4) \quad \frac{D_{\mathrm{m}}}{D_{\mathrm{p}}} = n$$

$$(5) \quad \frac{T_{\mathrm{m}}}{T_{\mathrm{p}}} = 1$$

$$(6) \quad \frac{S_{\mathrm{m}}}{S_{\mathrm{p}}} = n$$

where L represents the dimensions of the module, V and M are the volume and mass, respectively, of the roller module, D is the displacement of the module, T is the operating time and S is the operating speed, n is the geometric scale ratio, and the subscripts m and p denote the scale model and prototype (i.e., the full-size module), respectively.
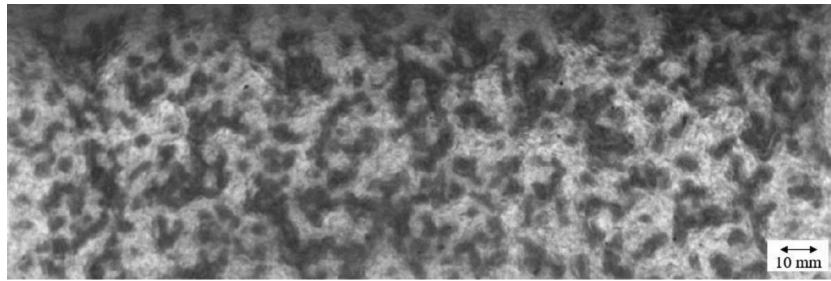
Therefore, according to eqs. 1–3, a series of tests was developed using two different weights of modules (3.64 and 5.46 kg), with identical dimensions of 115 mm × 115 mm × 100 mm (height × length × width). These two models are 1:13 scaled replicas of the four-sided, 8 and 12 t impact rollers (Broons BH-1300 and BH-1300 HD), respectively (Jaksa et al. 2019). In practice, an approximately 200 mm thick, crushed rock working base is typically placed at the ground surface of relatively loose, dry sandy soils to ensure the effective rotation and energy transfer of the roller, and to prevent it from bogging (Avalle and Carter 2005). In this study, a 0.2 mm thick, polyethylene membrane was placed on the upper surface of the transparent soil to simulate the working base used in the field to facilitate appropriate rotation of the module (Fig. 4c). This membrane is selected from various materials because it is thin enough to effectively transfer the energy from the module to the soil without compromising the accuracy of the tests. The membrane was loosely placed to allow pore water dissipation and compaction at the ground surface after several module passes.

As previously mentioned, two 1:13 scale models of the 8 and 12 t impact rollers were examined to study the relationship between the weight of the module and soil displacements. In addition, the number of rolling passes and the operating speed of both modules were varied to assess their effects on soil displacements. Operating speeds between 10 and 12 km/h are the most commonly adopted speeds in practical applications. However, the efficacy of RDC travels above 12 km/h has not been tested extensively in the field and, hence, the optimum speed for this type of roller has yet to be determined. Given that scale models are used in this study, prototype operating speeds were converted to scale model speeds, based on eqs. 4–6. Four different operating speeds are examined: 214, 256, 299, and 342 mm/s, corresponding to the prototype speeds of 10, 12, 14, and 16 km/h, respectively. Therefore, in total, eight tests were conducted for the 3.64 and 5.46 kg scale models at four different speeds, with each test being carried out up to 40 passes.

Calibration tests

The quality of the PIV results depends significantly on the development of a satisfactory speckled pattern. On the one hand, too many black-dyed particles can cause poor illumination and, hence, result in dark images. On the other hand, if too few black-dyed particles are used, the displacement information provided by the PIV results will be inadequate. Several calibration tests were performed to examine the optimum density (which is defined as the mass of coloured fused quartz particles divided by the area of the plane of interest) of the black-dyed fused quartz particles to form a speckled pattern within the plane of interest. The mean correlation coefficient obtained from the GeoPIV_RG software was used to quantify the optimum density of dyed particles as it reveals the correlation between images. As a result, a density of 1.5×10^{-3} g/mm^2 of black particles was found to be optimal as it yielded the highest correlation coefficient value. Figure 5 shows the speckled pattern formed by the optimal density of black particles viewed behind a 140 mm thickness of transparent soil. In the scale model test, the cross-sectional area of the plane of interest is 300 mm × 250 mm. Therefore, 112.5 g of dyed particles were used to form the speckled pattern in the tests. In addition, the optimum subset size was also investigated by repeating multiple PIV analyses with different subset sizes for each dyed particle density. Based on the highest mean correlation coefficient value, subsets of $6.52D_{50}$ (~25 mm) were selected to be used in the following PIV analyses. Each subset has a centroid spacing of 12.5 mm to preserve the accuracy of the PIV results. The scale model tests were conducted in a relatively dark

room, and the walls of the timber frame were painted black with a matte finish to minimize light reflection. To assess the efficacy of the apparatus and PIV system, the speckled pattern was captured over a time period where the test rig was non-operational, and no movement was obtained from the PIV results, which provided confidence in the setup and indicated that light reflection did not affect the test results.

Results and discussion

Soil displacement relative to module motion

Figure 6 presents the PIV results of successive images obtained from the first pass with the 3.64 kg module. A red marker is placed at one corner of the module to facilitate the analysis of the motion of the module. The operating speed of the 3.64 kg module is 256 mm/s, which, at the 1:13 scale, corresponds to a velocity of 12 km/h of the 8 t prototype. As the time interval in Fig. 6 is 0.23 s, the horizontal displacement of the module is approximately 59 mm in 0.23 s. The angular velocity is approximately 3.7 rad/s; therefore, the module rotates around its centre by 48.8° during the 0.23 s time period. The vectors in Fig. 6 have been scaled up by a factor of 8 to enhance the visualization of the soil displacements. In general, it can be seen that, as the module travels from right to left, the soil body displaces from right to left and from top to bottom, as one would expect. Figure 6a exhibits the displacement vectors prior to the module traversing the soil. Figure 6b shows the position of the module, illustrated at the correct scale with respect to the chamber, after it leaves the timber frame and contacts the transparent soil. The module subsequently traverses the upper surface of the soil (Figs. 6c, 6d, 6e, and 6f), which causes the particles beneath the module to displace downwards and to the left, i.e., in the same direction as the module's motion. The displacement vectors in Fig. 6c indicate that the soil particles are pushed in the direction of the module. The lower corner of the module in Fig. 6d penetrates into the soil, which causes the soil particles immediately beneath the ground surface to settle. In Fig. 6e, the soil behind the module displaces downwards and to the right, and the soil particles in front of the module are pushed to the left. In Fig. 6f, again, the soil in front of the module is pushed and displaces in the lateral direction of the module's motion. Figure 6g shows the cumulative displacement vectors after the first pass of the 3.64 kg module.

Figure 7 presents the cumulative horizontal and vertical displacements of regions A, B, C, D, E, and F (as shown in Fig. 6b) with respect to the time and motion of the 3.64 kg module in Fig. 6 for the first pass. To maintain consistency with the direction of motion shown in Fig. 6, the origin of the horizontal (time) axis in Fig. 7 is located on the right-hand-side of the plot. Positive horizontal displacements imply that the soil moves towards the right and positive vertical displacements refer to soil particles that displace downwards. Regions B, C, and D are at the same depth (i.e., 40 mm below the surface), but are, respectively, located on the left-hand-side, centre, and right-hand-side of the chamber.

Region A is located at the chamber's centreline, but at a depth of 17 mm, whereas regions E and F are located at the right-hand side of the chamber at depths of 100 and 160 mm, respectively. In general, and as expected, soil located in these regions undergoes compaction, as indicated by the significant displacements downwards and to the left when the roller impacts these areas. When the applied compactive force is removed, i.e., the module travels away from these two regions, the soil is slightly pushed upwards, which is consistent with behaviour observed in the field tests from Scott et al. (2019). They investigated the soil response during a single module impact and reported that the soil displaces downwards and may achieve its maximum vertical displacement due to loading. Then, the vertical displacement may decrease upon unloading. In terms of the module's influence, as it moves from right to left, region D is first examined. Between 0 and 0.23 s, it can clearly be seen that, when the module first impacts the soil near the right-hand boundary, the soil at region D is pushed to the left and downwards. Between 0.23 to 0.92 s, as the module continues to travel to the left, the soil slightly displaces upwards and to the right. After 0.92 s, there is no obvious displacement observed at region D, when the module has travelled further away from this location. At region C, from 0 to 0.46 s, the soil is mainly pushed horizontally in the direction of the module's motion. The soil shows its greatest downward displacements between 0.46 and 0.69 s as the module traverses close to region C, and then the soil moves upwards and to the right after 0.69 s because the module impacts the soil to the left of region C. As one would expect, the soil displacements at region A are similar to those that occur at C, because they are both located at the centreline of the chamber. However, the soil at region A has greater vertical displacements when compared with those at C, given that A is closer to the ground surface. Before 0.46 s, the particles at B displace slightly because of the motion of the module to the right of B, whereas between 0.46 and 0.92 s, the soil displaces upwards and to the left as the module approaches B. After 0.92 s, the soil gradually displaces to the right and downwards as the module continues to travel to the left-hand side of the chamber and then off the transparent soil and onto the timber frame. The values of cumulative displacements at 1.38 s show that, after the first pass of the module, the soil particles at regions B and C have permanently displaced downwards and to the right, and the soil located at A and D displaced downwards and to the left.

Figure 7b shows the cumulative displacements of regions E and F. It can be seen that the soil displacements at E are similar to those at D, but to a lesser extent, as they are located at the right-hand side of the chamber, with E being at a greater depth. As can be seen, the soil particles at region F experience no observable displacement during the first pass of the module given their depths below the ground surface.

To better understand the displacement patterns of the soil as a result of the module, the displacements of these regions are traced by plotting their x and y coordinates with respect to the time and motion of the module in Fig. 6 during the first pass; these displacements are also known as Eulerian trajectories

Fig. 6. Successive images of module motion: (*a*) *t* = 0 s, (*b*) *t* = 0.23 s, (*c*) *t* = 0.46 s, (*d*) *t* = 0.69 s, (*e*) *t* = 0.92 s, (*f*) *t* = 1.15 s, and (*g*) *t* = 1.38 s. [Colour online.]
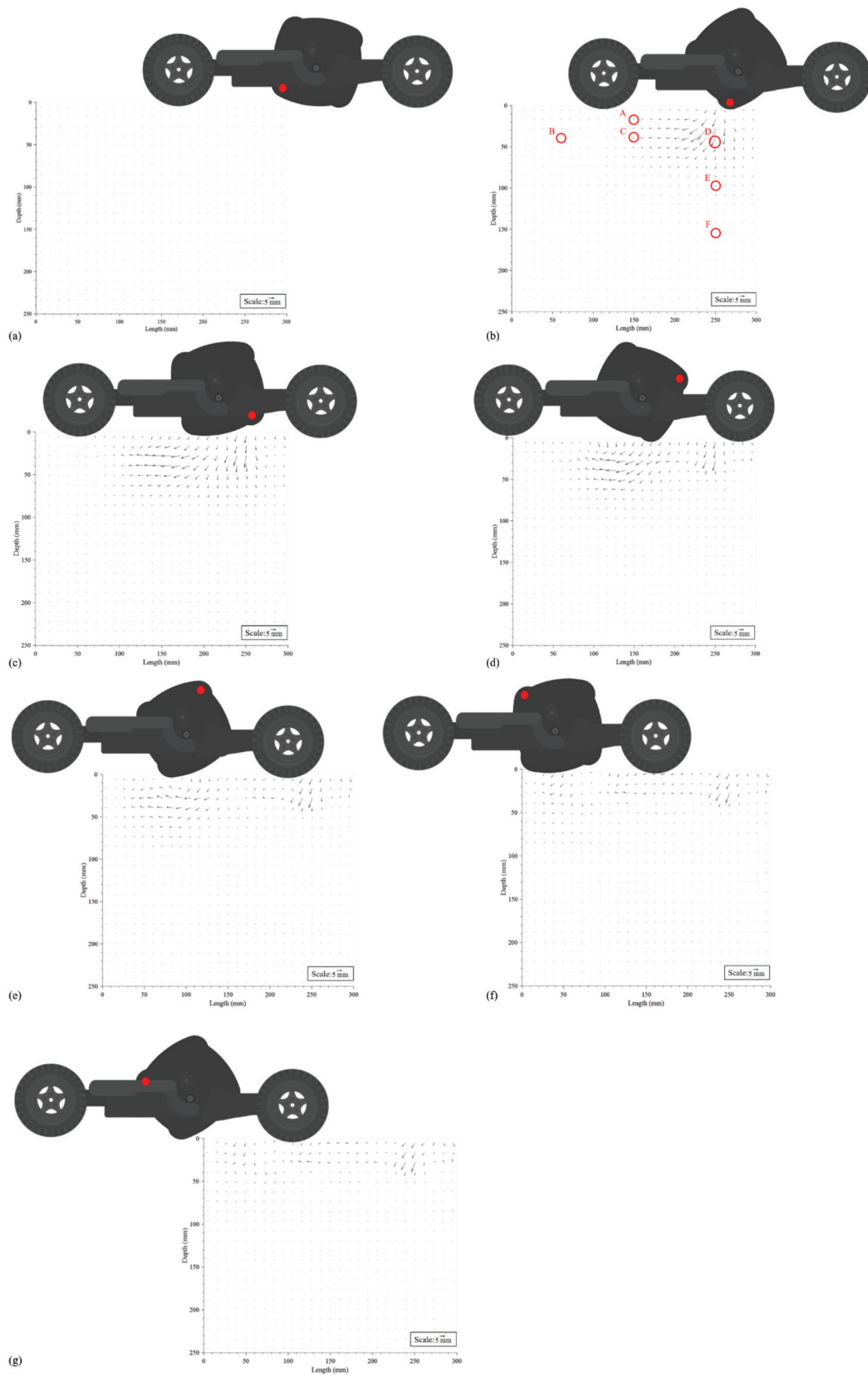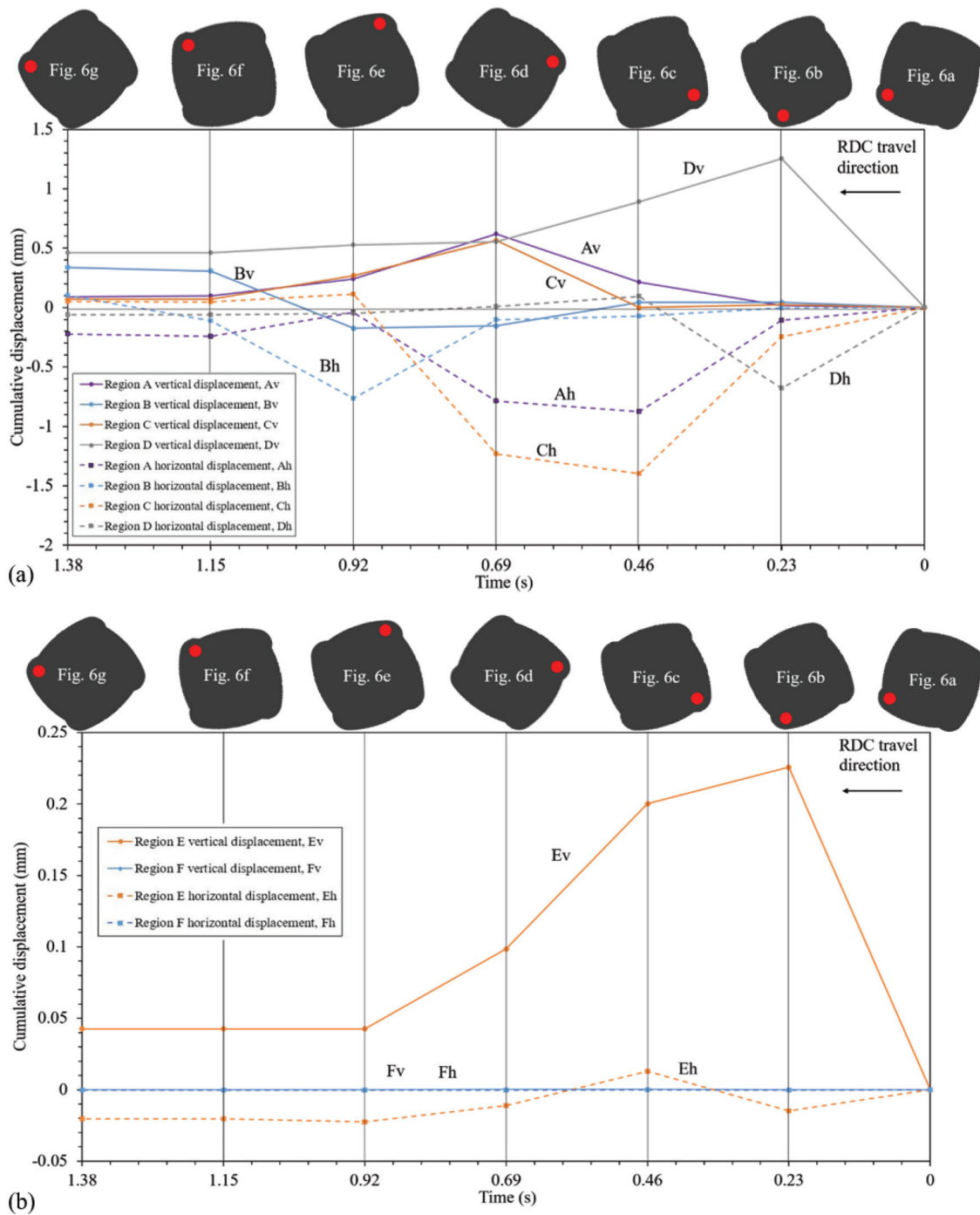
Fig. 7. Cumulative vertical and horizontal displacements of six regions versus time: (*a*) regions A, B, C, and D and (*b*) regions E and F, for first pass. [Colour online.]

(Omidvar et al. 2015). Similar to Fig. 6, the incremental displacements in Fig. 8 have been scaled up by a factor of 8 to reveal the movement of each region. Figure 8 shows the displacements of regions A, B, C, D, and E (refer to Fig. 6*b*). Note, to clearly observe the particle trajectories, the scales of both axes in each of these figures are different. As Fig. 7*b* shows that region F has no obvious vertical or horizontal displacement during the first pass of the module, the trajectories of region F are not included in Fig. 8. The red arrows point from the initial position towards the final position of the region (plastic displacements) and the black arrows indicate the movement of the region at different times (elastic displacements). The relative motion of the module is indicated in Figs. 6 and 7. It can clearly be seen that all these five regions displace significantly during the first pass of the module. When the module travels close to these regions, the soil in these regions moves to the left and downwards. As the module traverses away from these regions, the particles are pushed to the right and move upwards. If the soil is located near the ground surface (region A) or is directly impacted by the roller (regions D and E), the soil will exhibit greater horizontal displacements to the left than to the right. Therefore, the plastic displacements within these regions (shown by the red arrows) indicate that the soil in

Fig. 8. Trajectories of five regions during first pass of 3.64 kg module travelling at speed of 256 mm/s: (*a*) region A, (*b*) region B, (*c*) region C, (*d*) region D, and (*e*) region E. [Colour online.]
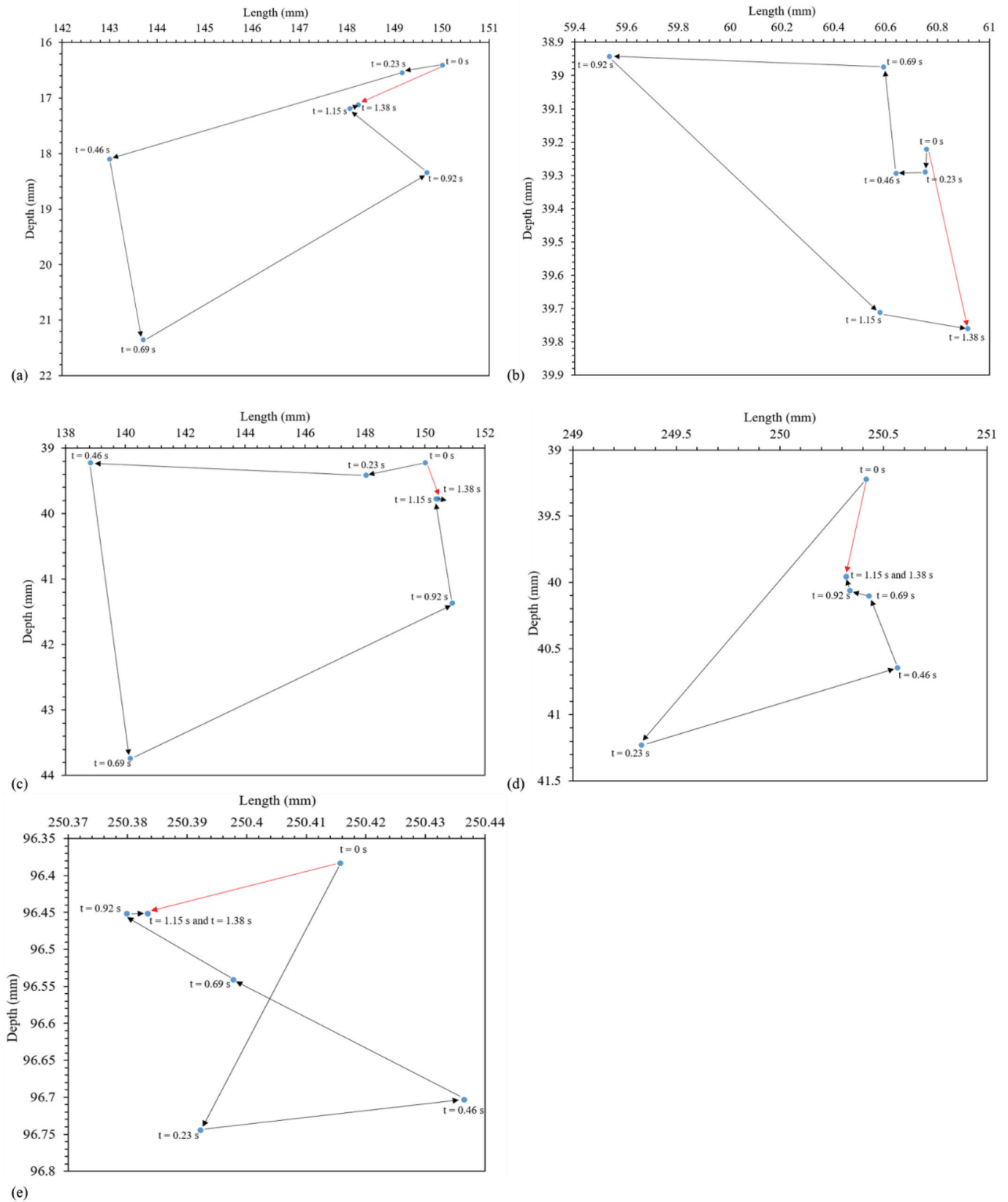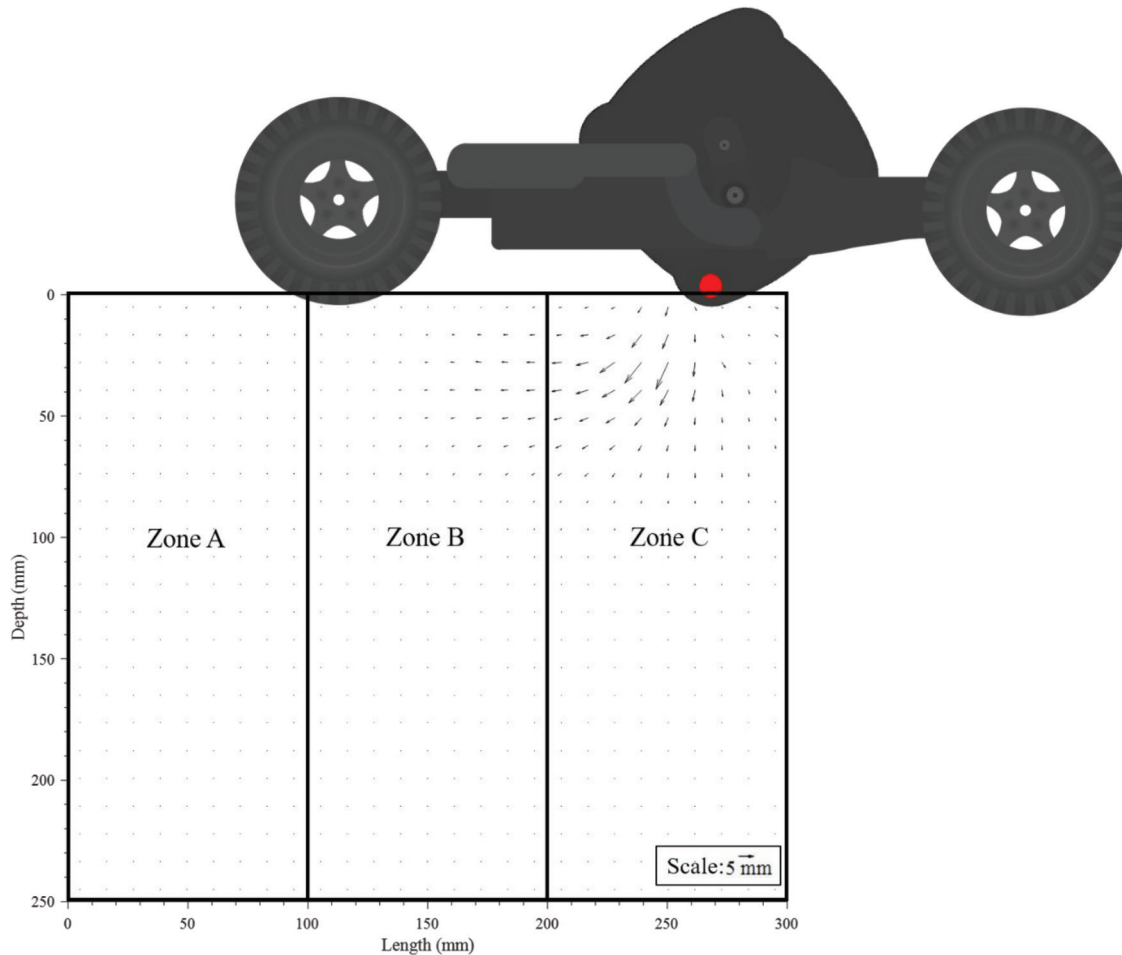
Fig. 9. Three subdivided zones of displacement field. [Colour online.]

these regions displaces to the left after the first pass. The soil particles at B and C exhibit slightly greater displacements to the right than to the left during the first module pass.

Module speed

The performance of the 3.64 and 5.46 kg modules, travelling at speeds of 214, 256, 299, and 342 mm/s, is examined using the displacements obtained from GeoPIV_RG. It can clearly be seen from Fig. 6c that the face of the module has rotated about its corner and compacted the soil, which is defined as the impact of the module. As the scale model impacts the transparent soil in the chamber, three or four times each pass, the front face of the chamber is divided into three zones, as shown in Fig. 9. It is worth mentioning that the roller may impact the soil in the same or a different location as the previous pass, because the roller is free to move along the track. However, in all tests, the first impact always occurs in zone C (e.g., Fig. 6b), and the second and third impacts occur in zones B and A (e.g., Figs. 6c and 6e), respectively. The fourth impact occurs near the left edge of zone A (e.g., Fig. 6f) or on the right edge of timber frame, depending on the speed of the module. Displacements induced by the module at zones A, B, and C are compared for both the 3.64 and 5.46 kg modules travelling at four different speeds to observe the repeatability or variation in the displacement patterns. Given that the soil movements in zones A and C are constrained by the edges of the chamber, the soil displacements from zone B are examined more extensively to investigate the behaviour of the module.

Cumulative displacement vectors and vertical displacement contours of soil subjected to the 3.64- and 5.46 kg modules,

travelling at four different speeds after 40 passes, are shown, respectively, in Figs. 10 and 11. In the vertical displacement contour plots, a positive value again suggests that the soil displaces downwards. Because of the use of the polyethylene membrane, the brightness of the images is compromised in some circumstances. This is demonstrated in Fig. 10d by the loss of vectors near the ground surface. The PIV results illustrate the variable nature of soil displacements near the ground surface. This is because the soil near the ground surface is disturbed and becomes undulating due to the geometry of the module. In general, it can clearly be seen that the displacement vectors and contours are significantly influenced by the operating speed of the module. As the operating speed increases, greater horizontal and vertical displacements are manifested. It is noted that the soil located above a depth of approximately 40 mm displaces downwards and to the left, whereas the soil below this depth displaces downwards and to the right. This phenomenon is similar to the cumulative displacement vectors obtained after the first pass of the 3.64 kg module (Fig. 6g), for the same reasons as explained above, and is more pronounced after 40 passes. In addition, it can be seen from the displacement contour plots that the vertical displacements induced by the module decrease with depth as the compactive energy dissipates with depth. As mentioned above, a medium-dense fused quartz sample, with larger particles (D_{50} = 3.84 mm), is used in this study, which results in the soil particles being less able to displace; therefore, the compactive effects are limited to relatively shallow soil depths.

To assess the behaviour of RDC, as well as other compaction methods, researchers and practitioners often refer to the improvement

Fig. 10. Cumulative displacement vectors (left) and vertical displacement contours (right) of 3.64 kg module after 40 passes at speeds of (*a*) 214 mm/s, (*b*) 256 mm/s, (*c*) 299 mm/s, and (*d*) 342 mm/s. [Colour online.]
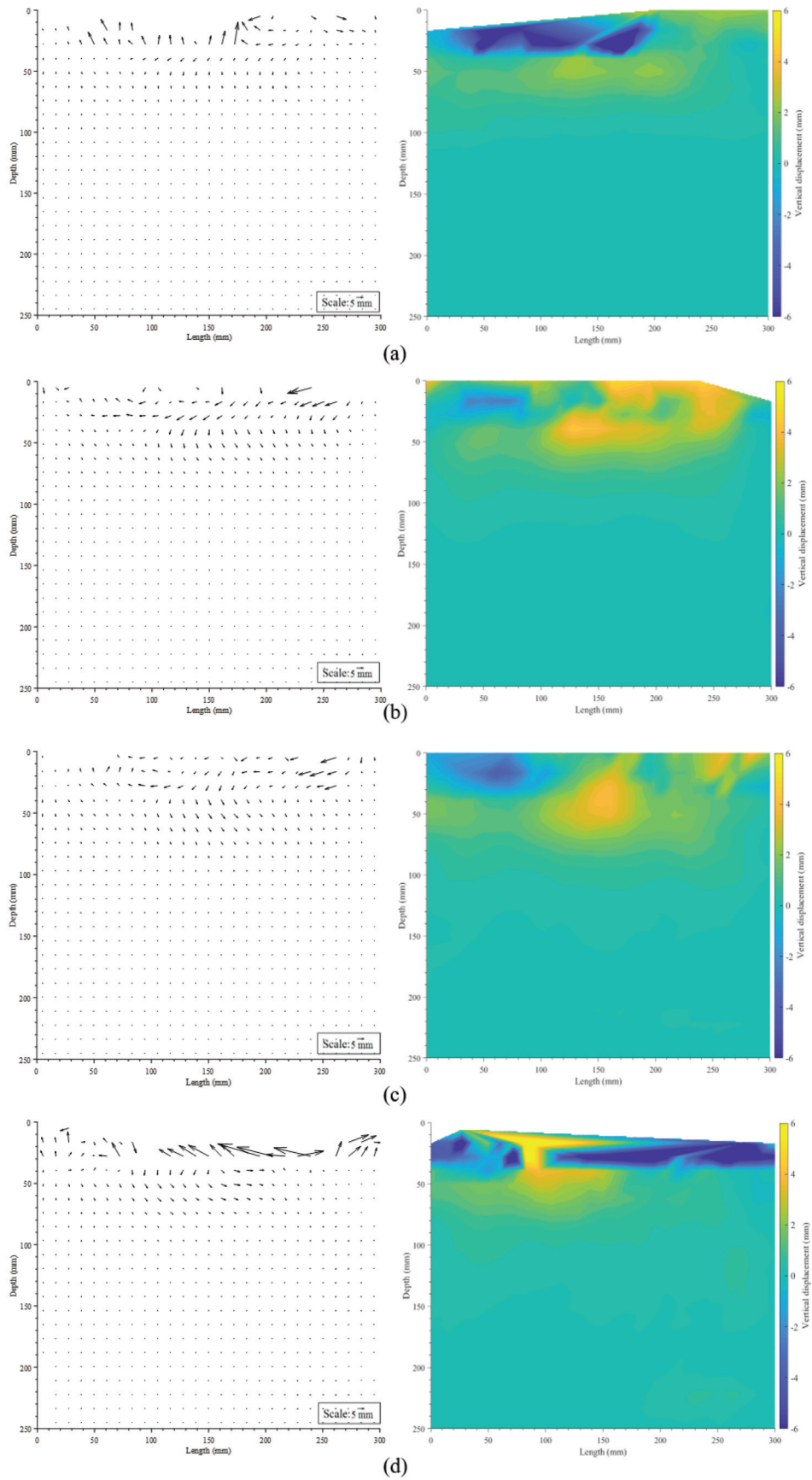

(a)

(b)

(c)

(d)

Fig. 11. Cumulative displacement vectors (left) and vertical displacement contours (right) of 5.46 kg module after 40 passes at speeds of (*a*) 214 mm/s, (*b*) 256 mm/s, (*c*) 299 mm/s, and (*d*) 342 mm/s. [Colour online.]
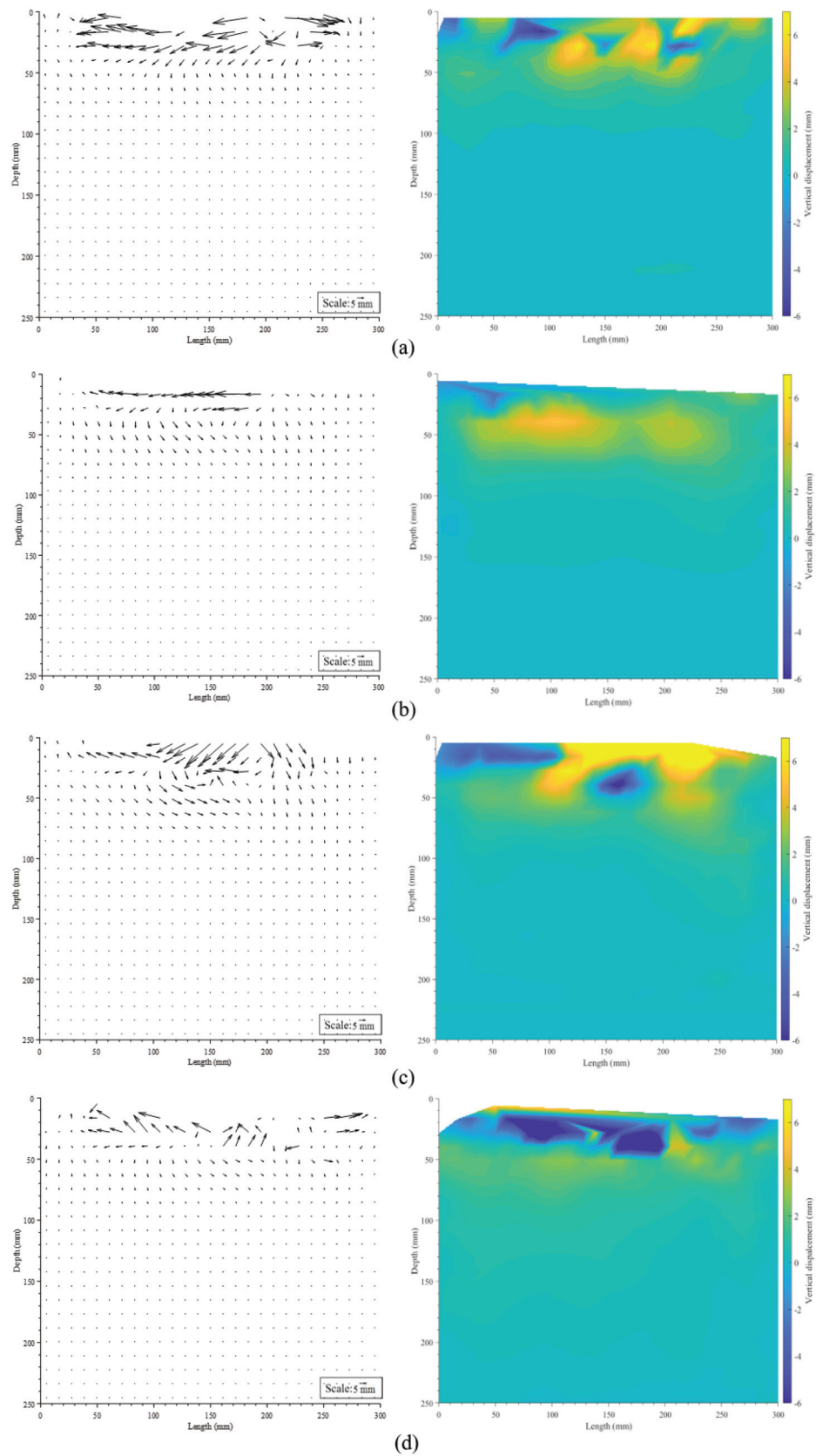
Table 1. Improvement depths of 3.64 and 5.46 kg modules at speeds of 214, 256, 299, and 342 mm/s.

Module weight (kg)	Operating speed (mm/s)	Improvement depth (mm)
3.64	214	130
	256	165
	299	230
	342	230
5.46	214	210
	256	220
	299	240
	342	230

depth (Kuo et al. 2013; Jafarzadeh 2006; Feng et al. 2015). Improvement depth is defined as the depth over which the soil's density and shear strength are improved by the applied compaction forces (Kuo et al. 2013; Jafarzadeh 2006). In this study, because the PIV technique is adopted, the improvement depth is quantified by the depth at which the soil undergoes vertical displacements less than 0.1 mm due to passing of the module. It is worth noting that the improvement depth is used merely as a surrogate to quantify the optimum speed for both the 3.64 and 5.46 kg modules. A plastic vertical displacement of 0.1 mm is adopted to represent the minimum quantifiable soil displacement considering the precision constraints of the adopted GeoPIV_RG algorithm (Stanier et al. 2016). From Table 1, it can be seen that, for the 3.64 kg scale model, as the operating speed increases, the improvement depth also increases. When the operating speed of the 3.64 kg module rises to 342 mm/s, the improvement depth shows no further increase. In addition, as shown by the displacement vectors plots (Fig. 10), when the 3.64 kg module travels at a speed of 214 mm/s, soil particles near the ground surface displace upwards and to the left due to sliding of the module. This phenomenon is consistent with observations reported by Avalle et al. (2009). They stated that the low operating speed may result in insufficient momentum to maintain module rotation without sliding. As the speed of the module increases, the soil particles beneath the ground surface are compacted and move downwards. The soil displacements increase as the operating speed rises. When the module travels at an operating speed of 342 mm/s, the soil near the ground surface is pushed upwards and to the left significantly due to the corners of the module. As reported by Clifford (1980), Avalle et al. (2009), and Scott et al. (2020), the module tends to bounce along the ground from corner to corner at higher operating speeds, which results in the soil near the ground surface being ploughed by the corner of the module. In addition, soil displacements at greater depths decrease when compared with the displacements induced by the module travelling at 299 mm/s. Soil displacements in zones A, B, and C both increase when the operating speed grows from 214 to 299 mm/s. When the module travels at 342 mm/s, soil displacements in zones A, B, and C reduce slightly.

As mentioned above, the soil in zone B has minimal influence from boundary effects, the average vertical displacements at different depths below the ground from this zone after 40 passes are plotted in Fig. 12 to assess the effects of operating speeds. The displacements of soil above 50 mm depth are not included in Fig. 12 as the soil above this depth is disturbed by the module, and results in somewhat random soil particle displacements. The dashed lines in Fig. 12 represent 0.1 mm soil displacement and assist in identifying the improvement depth shown in Table 1. In Fig. 12a, it can be seen that the average vertical displacements at different depths increase as the operating speed rises from 214 to 299 mm/s. When the 3.64 kg module is operated at 342 mm/s, the vertical displacements reduce significantly and the displacement at around 50 mm depth is even less than that which was measured at 214 mm/s. This is consistent with the findings from Rajarathnam et al. (2016). They stated that soil displacements increase as the operating speed rises until the module reaches its optimal velocity. Once the operating speed is greater than the optimal speed, soil displacements decrease. As a consequence, it can be concluded that, for the 3.64 kg module, an operating speed of approximately 299 mm/s is suggested as the optimal speed, from a compaction perspective.

Similar conclusions are obtained from the 5.46 kg module tests. As shown in Table 1, when the 5.46 kg scale model travels at a speed of 214 mm/s, the improvement depth is around 210 mm. The improvement depth increases as the operating speed grows. The results obtained from the 342 mm/s test show a decreased improvement depth. As seen in Fig. 11, with a 214 mm/s operating speed, the soil particles located above 50 mm depth move upwards and they are pushed in the direction of travel of the impact roller. When the roller operates at a 342 mm/s operating speed, the soil particles near the ground surface displace upwards significantly. As shown by the displacement vectors and vertical displacement contour plots, at a 299 mm/s speed, the module significantly compacts the soil located above 70 mm depth, as indicated by the downward displacements. When the module operates at 256 mm/s, the soil near the ground surface is ploughed in the direction of the impact roller, with no obvious vertical movement. The changes of soil displacements in zones A, B, and C for the 5.46 kg module travelling at four different speeds are similar to those observed for the 3.64 kg module. Displacements in zones A, B, and C increase when the speed of the roller rises from 214 to 299 mm/s, and the displacements in these zones decrease as the operating speed increases to 342 mm/s. In Fig. 12b, the vertical displacements in zone B increase as the operating speed rises from 214 to 256 mm/s. The 299 mm/s operating speed exhibits similar displacements as at 256 mm/s, but with a greater displacement at around 50 mm depth. The vertical displacements decrease when the operating speed rises to 342 mm/s. This is again consistent with the findings of Rajarathnam et al. (2016). Soil displacements increase as the operating speed rises to the optimal operating speed. After that, the soil displacements decrease. There are several reasons for this. Firstly, the module skips along the ground about its corners at higher operating speeds, and the compactive energy is delivered by the corners rather than the faces of the module, which results in the soil not being compacted effectively (Clifford 1980; Avalle et al. 2009; Scott et al. 2020). Secondly, the soil particles have insufficient time to rearrange at higher operating speeds; therefore, the soil has diminished plastic displacements (Rajarathnam et al. 2016). As with the 3.64 kg module, the test results indicate that 299 mm/s is the optimal speed for the 5.46 kg module, from a compaction standpoint.

Comparing the displacement fields caused by the 3.64 and 5.46 kg scale modules, the soil near the ground surface is pushed more dramatically in the direction of travel of the roller with respect to the 5.46 kg module. As the operating speed and material properties are identical for both the 3.64 and 5.46 kg modules, the heavier module produces a larger normal force and, hence, a greater friction force. Therefore, the 5.46 kg module causes the soil to move towards the left. In addition, according to the plots of the displacement vectors, the 5.46 kg module induces greater horizontal and vertical soil displacements for each operating speed, as one might expect. This conclusion is further supported by the average vertical displacement results in Fig. 12. The 5.46 kg module, operated at 214 mm/s, has similar vertical displacements to the 3.64 kg module operating at 256 mm/s, and the soil displacements measured with the 3.64 kg module travelling at 299 mm/s are smaller than those associated with the 5.46 kg module travelling at 256 mm/s. In general, the 5.46 kg module reaches better efficacy as it induces the greater improvement depth and larger soil displacements for each speed.

Fig. 12. Average vertical displacements at different depths within zone B after 40 passes: (*a*) 3.64 kg scale module and (*b*) 5.46 kg scale module. [Colour online.]
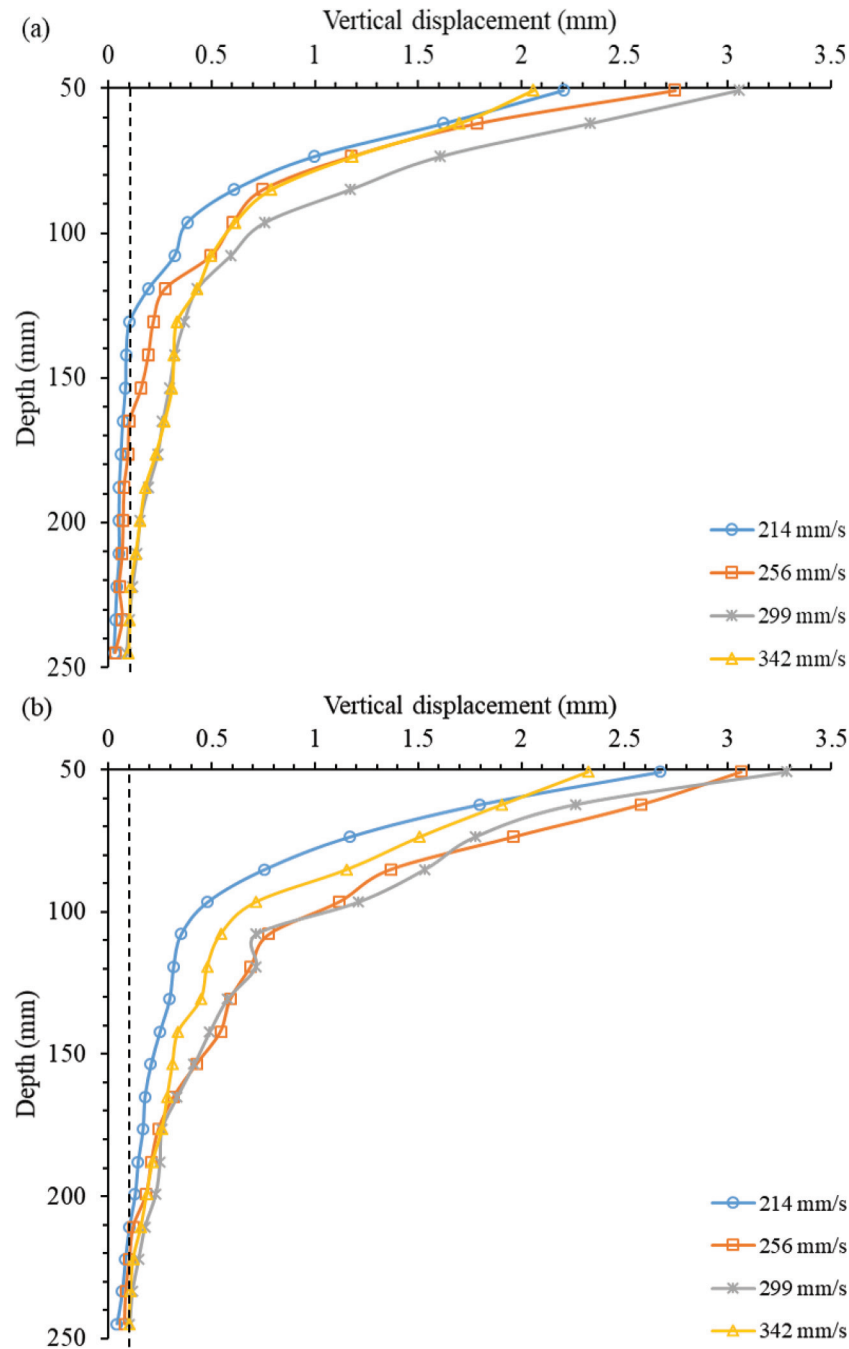

Optimum number of rolling passes

The optimum number of passes is determined by assessing the averaged vertical incremental displacements at 50 mm depth in zone B, because the soil at around 50 mm depth experiences the largest displacements, as shown by the vertical displacement contour plots for all eight tests (Figs. 10 and 11). Incremental particle displacements are obtained using the cumulative particle displacement data gathered from pass n minus those collected from pass $n - 1$. If the average vertical incremental displacement is less than 0.1 mm, it is assumed that no further quantifiable particle displacement occurs, acknowledging the limitations and resolution of the adopted GeoPIV_RG algorithm (Stanier et al. 2016).

As shown in Fig. 13, the most significant soil displacement generally occurs within the first 20 passes for both the 3.64 and 5.46 kg modules. With subsequent passes, the incremental soil displacement gradually decreases. In general, the incremental soil displacement is less than 0.1 mm after 35 passes. There is no obvious ground improvement after 35 passes. Therefore, for both the 3.64 and 5.46 kg modules, the optimum number of passes is around 35 passes, for the circumstances examined in the present paper.

Ground surface settlement

Three-dimensional (3D) ground surface scanning is applied as an advanced instrumentation technology to provide additional

Fig. 13. Average vertical incremental displacements at 50 mm depth within zone B: (*a*) 3.64 kg scale module and (*b*) 5.46 kg scale module. [Colour online.]
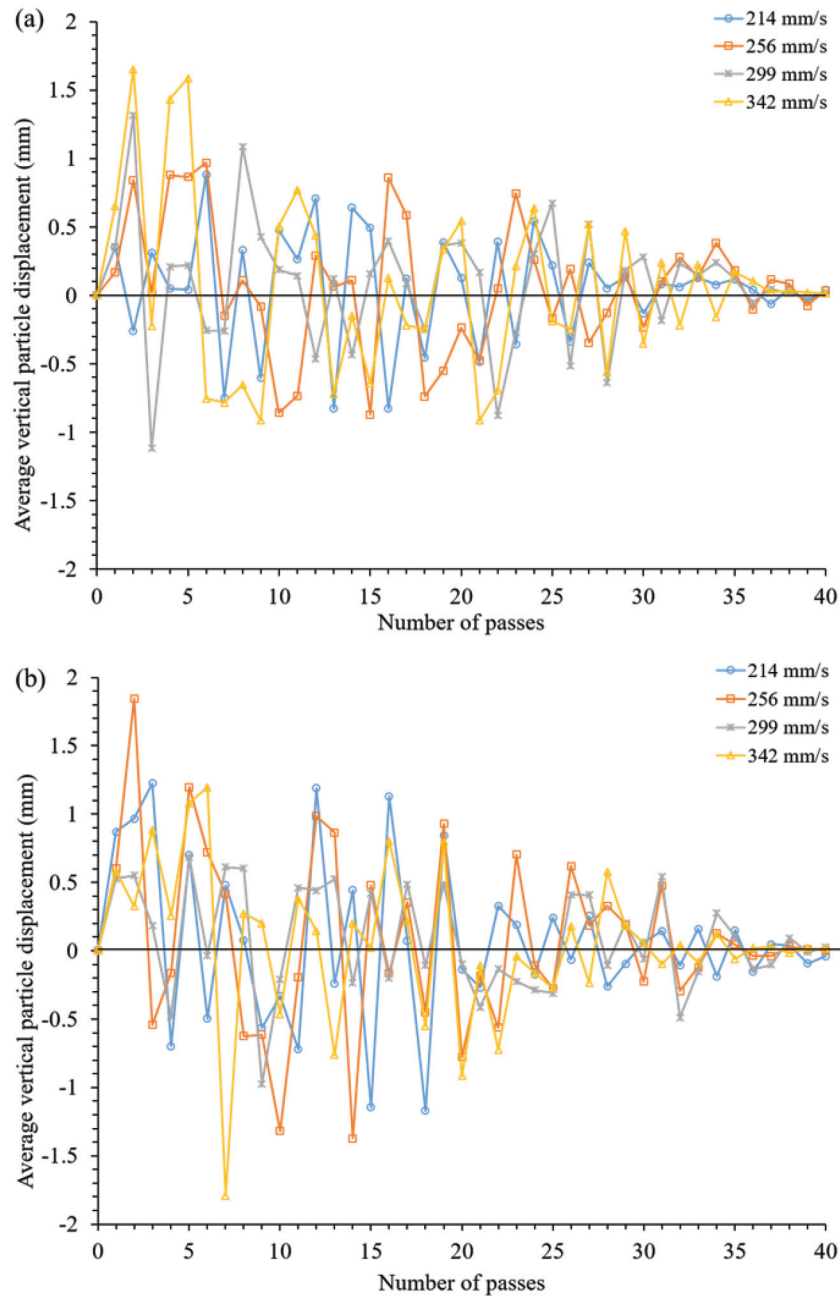
data to help understand the performance of the scale model. As the module produces non-uniform, undulating ground surface settlements, it is difficult to measure ground settlement efficiently and accurately by manual methods. A high-precision 3D surface scanner (EinScan Pro+) was adopted to provide measurements of the ground surface in high-resolution (distances between points are 0.2 to 3 mm in the point cloud). This technology employs non-laser, white light as the light source to generate a highly accurate (±0.05–0.3 mm) "point cloud" from the surface of an object in a very efficient manner (550 000 points per second) (Shining 3D 2019). To provide reference points for alignment, the process involves the use of adhesive reflective markers that are affixed on the timber frames and the ground surface of the transparent soil. To facilitate accurate measurement of the

ground surface by the 3D scanner, some of the pore fluid was removed using a syringe; otherwise, the ground surface was too transparent. After each scan, the pore fluid was carefully reinstated with the syringe. Examples of point clouds generated by the 3D surface scanner over the transparent surrogates are shown in Figs. 14*a* and 14*b*. The complete acrylic rectangular chamber adopted in the experiments is shown in Fig. 14. The yellow point cloud (Fig. 14*a*) is obtained prior to compaction by the 3.64 kg module and the blue point cloud (Fig. 14*b*) is the ground surface scanned after 40 passes of the 3.64 kg module at a speed of 256 mm/s. Figure 14*c* presents the superposition of both the yellow and blue point clouds to visualize more effectively the ground settlement induced by the module. In the regions where the yellow obscures the blue, this suggests that

Fig. 14. Point clouds obtained from 3D scanner: (*a*) initial ground surface, (*b*) after 40 passes, and (*c*) both superimposed. [Colour online.]
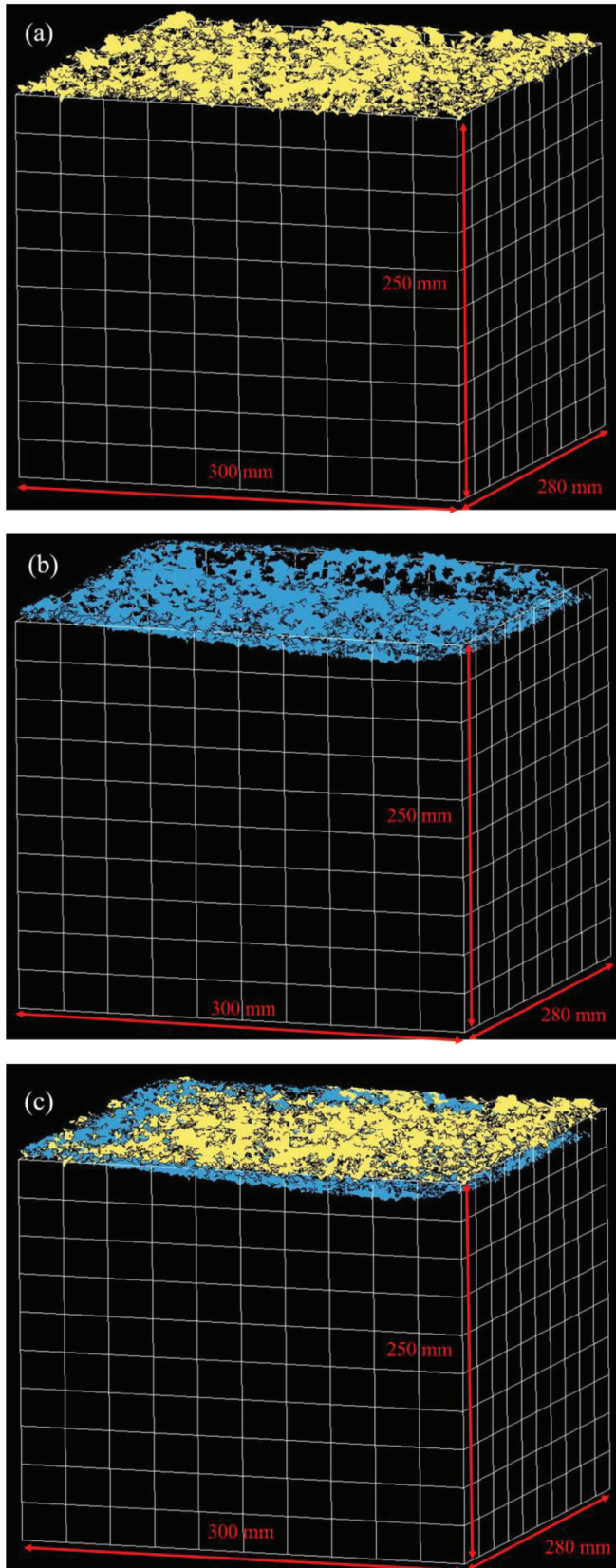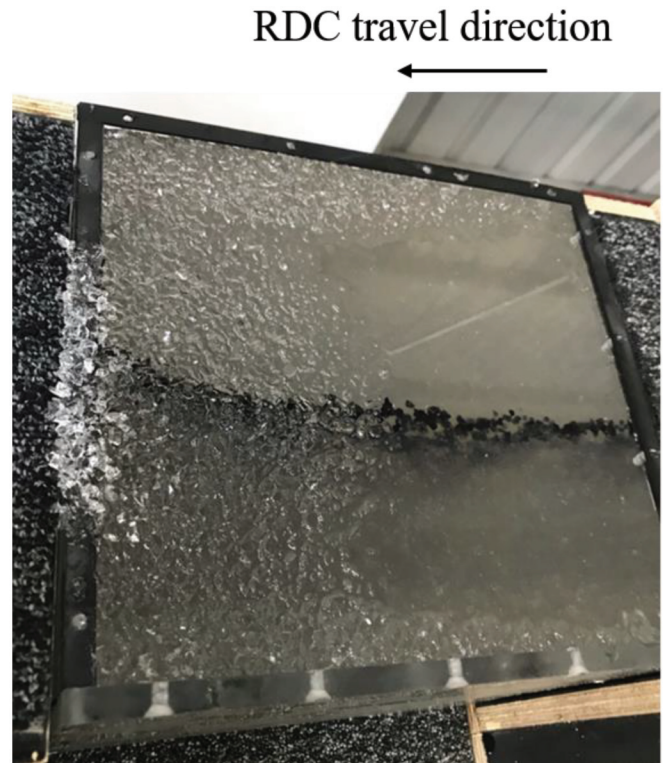

Fig. 15. Particle surface after 40 passes of 3.64 kg module travelling at 256 mm/s. [Colour online.]

the soil in these areas have displaced vertically below the initial ground surface. On the contrary, in the regions where the blue obscures the yellow, this implies that the soil has displaced vertically above the initial ground surface. It can be seen that the yellow (initial) point cloud is above the blue (after 40 passes) point cloud in the middle and in the right-hand side of the figure, which suggests that the soil in these regions has experienced vertical settlements after 40 passes, especially the soil at the right-hand side of the chamber, which shows significant settlements. The reason for this is that the roller module, in travelling from right to left, exits the timber frame and impacts the soil at the right of the chamber. As the roller traverses on the soil, the particles adjacent to the surface are pushed in the direction of the module's travel. Therefore, the soil accumulates to the left of the chamber, and the ground level here, after 40 passes, is higher than that prior to the module. Figure 15 shows a photograph of the ground surface of the transparent soil after 40 passes of compaction by the 3.64 kg module travelling at 256 mm/s. It can be seen that the soil at the right-hand side of the chamber has settled (as indicated by the pool of pore fluid at the surface) and the soil particles have accumulated at the left-hand side of the chamber, both of which are consistent with the 3D scanner results. In addition to providing visual comparisons of the ground surface induced by passing of the module, the 3D scanner also quantifies the extent of displacement of individual particles within the point cloud subsequent to the module. The displacement of each captured particle is summed and then averaged to obtain the average ground settlement with respect to the number of passes. Figure 16 shows the average ground settlement of zone B after every 10 passes. In general, as one would expect, the 5.46 kg scale model produces larger ground settlements when compared with the 3.64 kg module for each operating speed. The most significant settlements occur within the first 20 passes, for both the 3.64 and

Fig. 16. Average ground settlement results: (*a*) 3.64 kg scale module and (*b*) 5.46 kg scale module. [Colour online.]
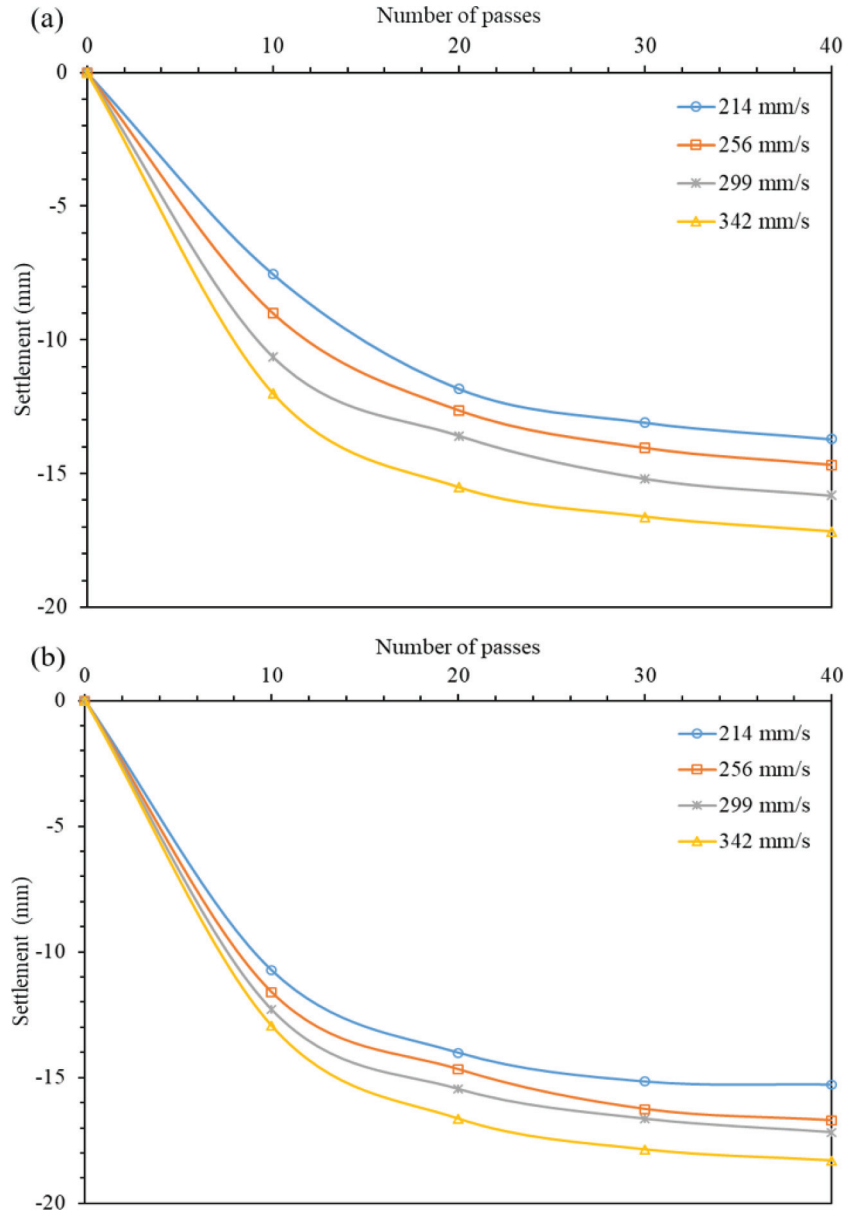
5.46 kg modules travelling at the four different speeds. The soil settlement increases modestly with subsequent passes. After 35 passes, the soil settlement at the ground surface shows minor improvement. This conclusion is in accord with that mentioned in the previous section. It can be observed that the higher operating speeds result in larger ground settlements due to greater kinetic and rotational kinetic energy induced by the module.

Summary and conclusions

This paper has presented a unique and novel physical modelling method, using transparent soil, a CCD camera, and the PIV technique, to study the mechanics and characteristics of rolling dynamic compaction (RDC). Two, 1:13 scale model replicas of the 8 and 12 t, four-sided impact rollers have been examined. The 5.46 kg module induces greater soil displacements when compared against the 3.64 kg module tested at four different speeds. For both the 3.64 and 5.46 kg modules, the optimal speed for

ground improvement is found to be approximately 299 mm/s. The most pronounced soil displacements occur within the first 20 passes and, subsequently, the soil displaces modestly. No obvious soil displacement is observed after 35 passes. A high-fidelity 3D scanner was employed to measure the ground settlement induced by the module. The value of the ground settlement exhibits an increasing trend with respect to rising operating speeds. Whilst the results of the present study are limited to a single initial density and particle-size distribution, the conclusions presented are nevertheless valuable in providing greater insight into RDC-influenced ground improvement and many of the factors that affect it.

from the School of Civil, Environmental and Mining Engineering at the University of Adelaide, especially Gary Bowman and Simon Golding, for their valuable assistance in the experimental work presented in this paper.

References

Adrian, R.J. 1991. Particle-imaging techniques for experimental fluid mechanics. Annual Review of Fluid Mechanics, **23**(1): 261–304. doi:10.1146/annurev.fl.23.010191.001401.

Ahmed, M., and Iskander, M. 2012. Evaluation of tunnel face stability by transparent soil models. Tunnelling and Underground Space Technology, **27**(1): 101–110. doi:10.1016/j.tust.2011.08.001.

Altaee, A., and Fellenius, B.H. 1994. Physical modeling in sand. Canadian Geotechnical Journal, **31**(3): 420–431. doi:10.1139/t94-049.

ASTM. 2017. Standard practice for classification of soils for engineering purposes (Unified Soil Classification System). ASTM standard D2487. American Society for Testing and Materials, West Conshohocken, Pa. doi:10.1520/D2487-17.

Avalle, D.L. 2006. Reducing haul road maintenance costs and improving tyre wear through the use of impact rollers. In Proceedings of the Mining for Tyres Conference, Perth, Australia. pp. 1–5.

Avalle, D.L. 2007. Ground vibrations during impact rolling. In Proceedings of the 10th Australia – New Zealand Conference (ANZ) on Geomechanics, Brisbane, Australia. pp. 1–6.

Avalle, D.L., and Carter, J.P. 2005. Evaluating the improvement from impact rolling on sand. In Proceedings of the 6th International Conference on Ground Improvement Techniques, Coimbra, Portugal, 18–19 July 2005. 8 pp.

Avalle, D.L., and Mckenzie, R.W. 2005. Ground improvement of landfill site using the square impact roller. Australian Geomechanics, **40**(4): 15–21.

Avalle, D.L., Scott, B.T., and Jaksa, M.B. 2009. Ground energy and impact of rolling dynamic compaction e results from research test site. In Proceedings of the 17th International Conference on Soil Mechanics and Geotechnical Engineering, Alexandria, Egypt, 5–9 October 2009. Vol. 3. pp. 2228–2231.

Bo, M.W., Na, Y.M., Arulrajah, A., and Chang, M.F. 2009. Densification of granular soil by dynamic compaction. Proceedings of the Institution of Civil Engineers – Ground Improvement, **162**(3): 121–132. doi:10.1680/grim.2009.162.3.121.

Bouazza, A., and Avalle, D.L. 2006. Effectiveness of rolling dynamic compaction on an old waste tip. In Proceedings of the 5th ICEG Environmental Geotechnics: Opportunities, Challenges and Responsibilities for Environmental Geotechnics: Proceedings of the ISSMGE's 5th International Congress, Cardiff City Hall, Cardiff, Wales, UK, 26–30 June 2006. pp. 1–7.

Bransby, P., and Milligan, G. 1975. Soil deformations near cantilever sheet pile walls. Géotechnique, **25**(2): 175–195. doi:10.1680/geot.1975.25.2.175.

Carvalho, T., Suescun-Florez, E., Omidvar, M., and Iskander, M. 2015. A nonviscous water-based pore fluid for modeling with transparent soils. Geotechnical Testing Journal, **38**(5): 805–811. doi:10.1520/GTJ20140278.

Chung, O.Y., Scott, B.T., Jaksa, M.B., Kuo, Y.L., and Airey, D. 2017. Physical modeling of rolling dynamic compaction. In Proceedings of the 19th International Conference on Soil Mechanics and Geotechnical Engineering, Seoul, Korea, 18–22 September 2017. pp. 905–908.

Clifford, J.M. 1980. The development and use of impact rollers in the construction of earthworks in southern Africa. CSIR Report 373. National Institute for Transport and Road Research, Pretoria, South Africa.

Feng, S.J., Du, F.L., Shi, Z.M., Shui, W.H., and Tan, K. 2015. Field study on the reinforcement of collapsible loess using dynamic compaction. Engineering Geology, **185**: 105–115. doi:10.1016/j.enggeo.2014.12.006.

Iskander, M. 2010. Modelling with transparent soils: visualizing soil structure interaction and multi phase flow, non-intrusively. Springer-Verlag Berlin Heidelberg. ISBN-13: 978-3642025006.

Jafarzadeh, F. 2006. Dynamic compaction method in physical model tests. Scientia Iranica, **13**(2): 187–192.

Jaksa, M.B., Scott, B.T., Mentha, N.L., Symons, A.T., Pointon, S.M., Wrightson, P.T., and Syamsuddin, E. 2012. Quantifying the zone of influence of the impact roller. In Proceedings of ISSMGE-TC 211 International Symposium on Ground Improvement, Brussels, Belgium, 30 May–1 June 2012. Vol. 2. pp. 41–52.

Jaksa, M.B., Airey, D.W., Scott, B.T., Kuo, Y.L., Ranasinghe, T., Bradley, A.C., et al. 2019. Quantifying the effect of rolling dynamic compaction. In Proceedings of the 4th World Congress on Civil, Structural, and Environmental Engineering (CSEE'19), Rome, Italy, 7–9 April 2019. doi:10.11159/icgre19.1.

Kuo, Y.L., Jaksa, M.B., Scott, B.T., Bradley, A.C., Power, C.N., Crisp, A.C., and Jiang, J.H. 2013. Assessing the effectiveness of rolling dynamic compaction. In Proceedings of the 18th International Conference on Soil Mechanics and Geotechnical Engineering, Paris, France, 2–6 September 2013. Vol. 2. pp. 1309–1312.

Li, Y., Airey, D., and Jaksa, M. 2021. Evaluating the effective depth of rolling dynamic compaction with a three-sided compactor. International Journal of Physical Modelling in Geotechnics. doi:10.1680/jphmg.20.00079.

Liu, J. 2009. Visualizing 3-D internal soil deformation using laser speckle and transparent soil techniques. In Proceedings of Characterization, Modeling, and Performance of Geomaterials: GeoHunan International Conference 2009, Changsha, Hunan, China, 3–6 August 2009. Geotechnical Special Publication 189. pp. 123–128. doi:10.1061/41041(348)18.

Liu, J., and Iskander, M.G. 2010. Modelling capacity of transparent soil. Canadian Geotechnical Journal, **47**(4): 451–460. doi:10.1139/T09-116.

Liu, J., Liu, M., and Gao, H. 2010. Influence of pile geometry on internal sand displacement around a laterally loaded pile using transparent soil. In Proceedings of Deep Foundations and Geotechnical In Situ Testing, GeoShanghai International Conference 2010, Shanghai, China, June 3–5 2010. American Society of Civil Engineers, Reston, Va. pp. 104–110. doi:10.1061/41106(379)12.

Mandava, S.S., Watson, A.T., and Edwards, C.M. 1990. NMR imaging of saturation during immiscible displacements. AIChE Journal, **36**(11): 1680–1686. doi:10.1002/aic.690361108.

Omidvar, M., Chen, Z., and Iskander, M. 2015. Image based lagrangian analysis of granular kinematics. Journal of Computing in Civil Engineering, ASCE, **29**(6): 04014101. doi:10.1061/(ASCE)CP.1943-5487.0000433.

Pak, A., Shahir, H., and Ghassemi, A. 2005. Behavior of dry and saturated soils under impact load during dynamic compaction. In Proceedings of 16th International Conference on Soil Mechanics and Geotechnical Engineering, Osaka, Japan, 12–16 September 2005. pp. 1245–1248.

Pinard, M. 1999. Innovative developments in compaction technology using high energy impact compactors. In Proceedings of the 8th Australia New Zealand Conference on Geomechanics: Consolidating Knowledge. Australian Geomechanics Society, Barton, Australia. pp. 775–781.

Posadas, D., Tannus, A., Panepucci, H., and Crestana, S. 1996. Magnetic resonance imaging as a non-invasive technique for investigating 3-D preferential flow occurring within stratified soil samples. Computers and Electronics in Agriculture, **14**(4): 255–267. doi:10.1016/0168-1699(95)00032-1.

Rajarathnam, P., Airey, D.W., Masoudian, M.S., and Jaksa, M.B. 2016. Model tests of rolling dynamic compaction. In Proceedings of the 19th Southeast Asian Geotechnical Conference and 2nd AGSSEA Conference, Kuala Lumpur, 31 May – 3 June. pp. 505–510.

Scott, B., and Jaksa, M. 2014. Evaluating rolling dynamic compaction of fill using CPT. In Proceedings of the 3rd International Symposium on Cone Penetration Testing (CPT'14), Las Vegas, NV, 12–14 May 2014. pp. 941–948.

Scott, B., Jaksa, M., and Kuo, Y. 2012. Use of proctor compaction testing for deep fill construction using impact rollers. In Proceedings of the International Conference on Ground Improvement and Ground Control, Wollongong, Australia, 30 October–2 November 2012. pp. 1107–1112. doi:10.3850/978-981-07-3560-9_04-0412.

Scott, B., Jaksa, M., and Syamsuddin, E. 2016. Verification of an impact rolling compaction trial using various in situ testing methods. In Proceedings of the 5th International Conference on Geotechnical and Geophysical Site Characterisation, Gold Coast, Queensland, Australia, 5–9 September 2016. pp. 735–740.

Scott, B.T., Jaksa, M.B., and Mitchell, P.W. 2019. Ground response to rolling dynamic compaction. Géotechnique Letters, **9**(2): 99–105. doi:10.1680/jgele.18.00208.

Scott, B.T., Jaksa, M.B., and Mitchell, P.W. 2020. Influence of towing speed on effectiveness of rolling dynamic compaction. Journal of Rock Mechanics and Geotechnical Engineering, **12**(1): 126–134. doi:10.1016/j.jrmge.2019.10.003.

Shining 3D. 2019. User manual: EinScan-Pro 2X/2X Plus/EP EXScan Pro Software V.3.3. Available from https://it3d.com/wp-content/uploads/download-files/manual/en/EXScan-Pro-User-Manual-V3.3.0.2.pdf [Accessed 12 October 2019].

Stanier, S.A., Blaber, J., Take, W.A., and White, D. 2016. Improved image-based deformation measurement for geotechnical applications. Canadian Geotechnical Journal, **53**(5): 727–739. doi:10.1139/cgj-2015-0253.